Study of Fluidization Behavior Transition from Geldart B to A Induced by High Temperature Using Electrical Capacitance Tomography

Kai Huang, Shuanghe Meng, Tao Zhang, Mao Ye,* Wuqiang Yang, and Zhongmin Liu

Read Online

ACCESS | Metrics & More | Article Recommendations

ABSTRACT: The transition of the fluidization behavior of Geldart B particles to that of A particles induced by temperature change was investigated by a developed high-temperature electrical capacitance tomography (ECT) sensor. Silica particles with a Sauter mean diameter of 237 μm and density of 2650 kg/m^3, typically Geldart B particles under ambient conditions, were fluidized in a column of 5.5 cm from 20 to 600 °C. With the increase in temperature, ECT measurements showed a decrease in minimum bubbling velocity (U_{mb}), no bed expansion characteristic in the homogeneous fluidization regime, an absence of multiple-bubbles regime, and a larger bubble size. The pressure drop against superficial gas velocity curves at elevated temperatures confirmed homogeneous fluidization between the minimum fluidization velocity (U_{mf}) and U_{mb}. Our analysis demonstrates that cohesive interparticle forces, which increase linearly with temperature, are responsible for the fluidization behavior transition of the silica particles.

Geldart group B particle behavior → Geldart group A particle behavior
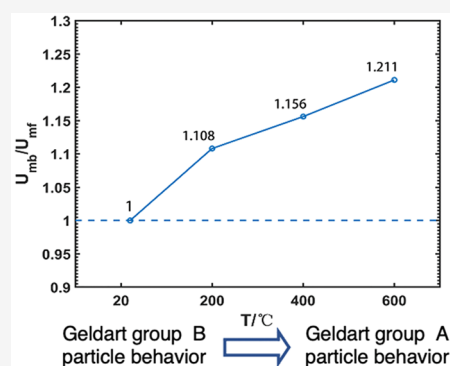
1. INTRODUCTION

Gas–solids fluidized bed reactors operated at high temperatures are widely employed in industrial processes, including methanol-to-olefins (MTO),[1] polymerization,[2,3] coal combustion,[4,5] and metallurgy[6] due to their excellent performance in heat and mass transfer. However, it has been discovered that fluidization behaviors at high temperatures can be changed due to the growth of particle agglomeration, which in severe cases can lead to defluidization, and the growth of particle agglomeration can be attributed to the increase in interparticle cohesive forces induced by the temperature effects.[2-7] For example, in the polymerization fluidized bed rectors, small polymer particles tend to stick together or wall and form large agglomerates due to attractive forces, including chain entanglement, electrostatic forces, and van Der Waals forces.[2,3] In metallurgy processes, like the production of metallic iron by iron ore with gas reductants, particle agglomerations are due to the sintering forces of precipitated iron.[6] Therefore, a proper understanding of the changes in fluidization behaviors at high temperatures is essential for the design, operation, and optimization of gas–solids fluidized bed reactors.

Geldart classified particles into four groups based on density difference and particle size in gas–solids fluidization, namely, Geldart A, B, D, and C particles.[8] The fluidization behaviors of these particles vary prominently. For Geldart A particles, the bed expands gradually with increasing superficial gas velocity before reaching the minimum bubbling velocity, which is known as the homogeneous fluidization regime. As the

superficial gas velocity increases, the bed commences bubbling with relatively small bubbles, resulting in smooth fluidization and reduced gas bypassing.[8,9] In the case of Geldart B particles, bubbles initially appear when the bed starts fluidization, and the bubble coalesces with the bed height, increasing gas bypassing and reducing solids mixing.[8,9] For Geldart C particles, powders lift as a plug in small diameter tubes or channels, while for Geldart D particles, large bubbles occur when they are fluidized, and the bed can be made to spout.[8] Mostoufi's research has further extended the classification of powders by taking into account the interparticle forces acting upon them.[10] The results have aligned with the Geldart classification, highlighting that these forces are the primary determinant of particles' fluidization characteristics.

In the past decades, researchers have examined the effect of temperature on fluidization transition behaviors between different Geldart groups. Due to a lack of satisfactory measurement techniques at high temperatures, most previous works were conducted based on indirect measurements, such as pressure or pressure drop through a fluidized bed. For instance, Botterill et al.[11] measured the pressure drop of
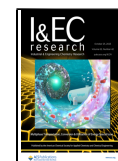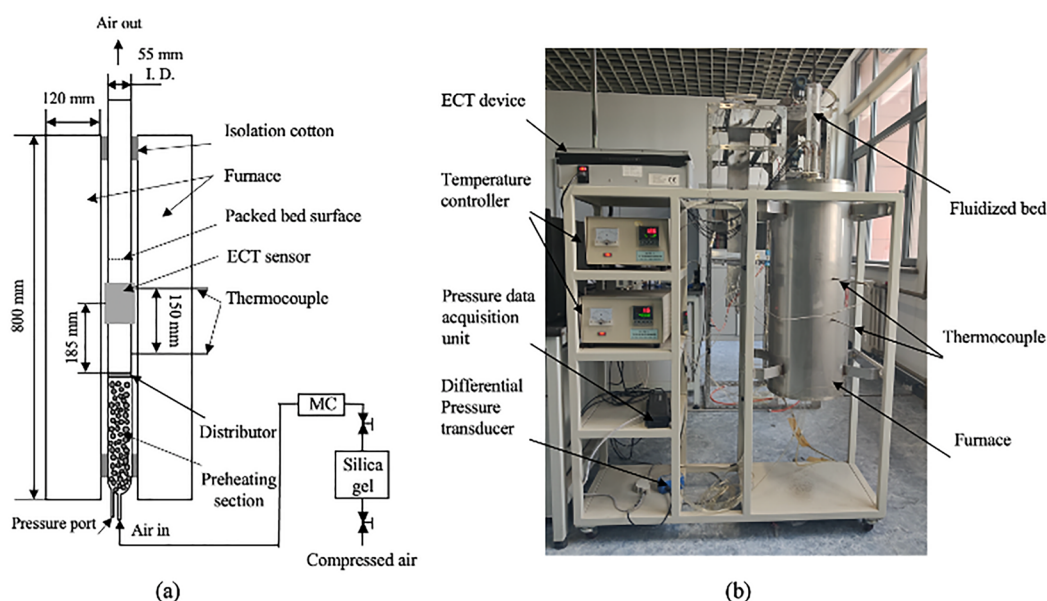
Figure 1. Experimental facility, including a fluidized bed equipped with a high-temperature ECT sensor, (a) schematic diagram, (b) photo of the experimental facility.

fluidized beds filled with sand between 380 and 2320 μm up to 960 °C and found that, for particles between 380 and 530 μm, the void fraction at incipient fluidization increases with temperature. Lucas et al.[12] confirmed an increase in the minimum fluidization void fraction with rising temperature for particles with a narrower size distribution based on the pressure drop measurement. Lettieri et al.[13] measured pressure drop across a fluidized bed and standard collapse time to compare the fluidization behavior of FCC catalysts from ambient conditions up to 650 °C. They found that the increasing temperature had an effect on both hydrodynamic and interparticle forces and resulted in a shift of fluidization behavior from Geldart A to C in the fluidized bed. Shabanian and Chaouki[14] studied the fluidization of coarse particles at high temperatures from 700 to 1000 °C by pressure measurements. They revealed that gas density principally impacts the bubbling fluidization of coarse particles at high temperatures if the cohesive interparticle forces are negligible. They also highlighted the change in physical or physicochem-ical properties of both the fluidized particles and gas due to a rise in temperature. Xu et al.[15] investigated the fluidization behavior of Geldart group D particles (i.e., corundum particles) at extremely high temperatures up to 1600 °C. They discovered that the increase in thermally induced interparticle forces caused the particles to exhibit a similar fluidization behavior as group B or even group A particles. In addition to pressure measurements, Cui et al.[16] utilized an optical fiber probe to measure the local and average void fractions of the dense phase to investigate the fluidization behavior transition from Geldart A to B for FCC particles in a range of 25−420 °C. They showed that an increase in temperature could cause fluidization behavior transition from Geldart A to B, which they attributed to the enhanced interparticle attractive forces and decreased interparticle repulsive forces. Based on the above discussions, especially when comparing the characteristics of FCC particles measured by Lettieri et al.[13] and Cui and Chaouki,[16] it is apparent that contradictory conclusions were presented. This highlights the difficulty in accurately measuring fluidized bed characteristics

at high temperatures and the limitations of indirect measure-ment methods, such as pressure transducers and optical fiber probes.

Visualization of fluidized bed behaviors at high temperatures is critical for studying fluidization transition, especially for the onset of bubbles in a fluidized bed as the minimum bubbling fluidization is widely accepted as the point at which the first visual bubble appears. Raso et al.[17] designed a two-dimensional (2D) fluidization facility inside an electrically heated refractory furnace and applied a video camera to record the fluidization processes up to 900 °C. They confirmed the existence of a looser stable structure in the fluidized bed even at zero gas velocity, induced by enhanced interparticle forces at high temperatures. Formisani et al.[18] further explored the origin of the increase in the void fraction of a packed bed due to the temperature and argued that it is related to the variation in interparticle forces with temperature; a classical correlation can be directly applied if the dependence of void fraction on temperature is properly included. However, these results were derived from visualizations of 2D fluidized beds, which may differ from those observed in three-dimensional (3D) beds where optical imaging is more difficult. Recently, Chirone et al.[19] used an X-ray imaging system along with pressure measurements to study the effect of temperature up to 500 °C on the minimum fluidization velocity of different Geldart powders (B, A, and C) in a 3D fluidized bed of 140 mm diameter. The X-ray images captured the flow structures, such as the gas channels. Nevertheless, the low temporal resolution and high cost of the X-ray imaging system hinder its application in the industry.

Electrical capacitance tomography (ECT) based on capacitance measurement is a visualization technique widely used to measure the hydrodynamics of 3D fluidized beds, particularly solid fraction distribution, bubble size, and bubble rise velocity.[20−23] However, ECT has been mainly used at ambient temperature because of the challenges in making high-temperature ECT sensors and in dealing with the effect of temperature on capacitance measurements and image reconstruction. We have successfully developed high-temper-
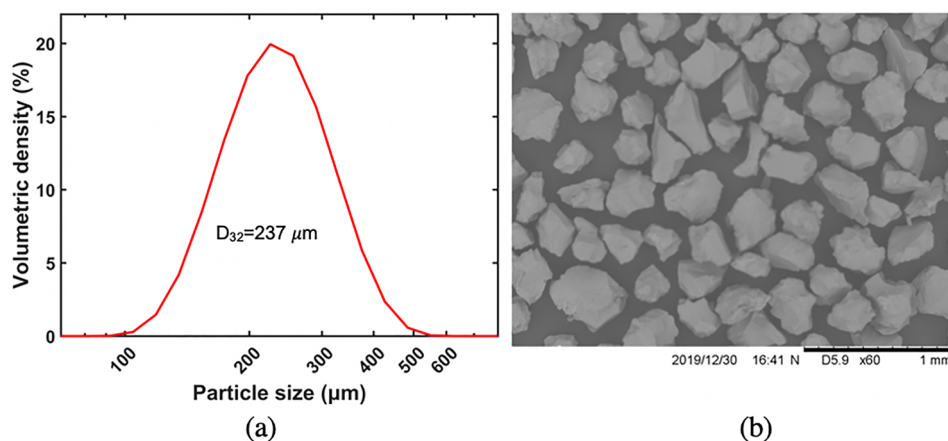
Figure 2. (a) Particle size distribution and (b) SEM images.

ature ECT sensors, which can withstand up to 1000 °C,[24,25] and showed that the high-temperature ECT could work well with fluidized beds up to 800 °C.[26] Wang et al.[27] also extended the application of high-temperature ECT to measure a slugging fluidized bed of Geldart D particles to 650 °C. The invention of high-temperature electrical capacitance tomography has provided a novel method for detecting the characteristics of a high-temperature fluidized bed.

Therefore, in this paper, we conducted an experimental study on the fluidization behaviors of silica particles with a mean diameter of 237 μm and a density of 2650 kg/m^3, typically of Geldart B powder under ambient conditions, using a 55 mm inner diameter fluidized bed equipped with a high-temperature ECT sensor. We varied the temperature from 20 to 600 °C and analyzed the resulting changes in fluidization characteristics, including minimum bubbling velocity/minimum fluidization velocity (U_{mb}/U_{mf}), bubble characteristics, and average solid fraction against superficial gas velocity, using electrical capacitance tomography (ECT) and differential pressure measurements. Our results revealed a transition in fluidization behavior from Geldart B to A of silica particles, and we also analyzed the reasons behind this transition.

2. EXPERIMENTAL SECTION

Figure 1 shows the experimental setup which consists of a fluidized bed with a high-temperature ECT sensor capable of reaching temperatures up to 800 °C.[26] The furnace depicted in the figure has dimensions of 800 mm in length and 120 mm in thickness, with an inner diameter of 80 mm for heating fluidized beds. To regulate the heating process, we affixed two thermocouples 15 cm apart onto the outside wall of the fluidized bed. Insulation cotton was used at both ends of the furnace to minimize the gap between the fluidized bed and the inner wall, thus reducing heat loss by convection. In our actual measurements, we first measured the packed bed height (around 25 cm at different temperatures) and adjusted the vertical position of the packed bed to ensure that its vertical center is aligned with the furnace's midpoint. Consequently, the apparatus's design ensures a stable temperature environment for measuring the fluidized bed.

We conducted meticulous experiments with the same amount of silica particles (780 g) at various temperatures (20, 200, 400, and 600 °C). To ensure consistent superficial gas velocity increments (0.1 cm/s) between the packed bed and the slugging bed at each temperature, we adjusted the gas

volumetric flow rate based on the ideal gas equation. Before the measurements, we calibrated the ECT system by utilizing normalized capacitance vectors (λ) as shown in eq 1 to reconstruct the normalized permittivity distribution.[28]

$$\lambda = \frac{C - C_L}{C_H - C_L} \tag{1}$$

Here, C is the measurement result, C_L and C_H are the results corresponding to the empty bed and packed bed, respectively. To ensure the packed bed reached the set temperature, we heated the empty column to the desired temperature and allowed sufficient time for it to equilibrate, thereby reducing temperature fluctuations to within 0.2 °C, as observed by the thermocouples. We measured the pressure drops across the empty column at various superficial gas velocities and calibrated the ECT system using a low-permittivity material (air) to obtain the low capacitance value (C_L). Next, we introduced 780 g of silica particles into the empty bed and increased the superficial gas velocities gradually until the bed was vigorously fluidized and maintained at the set temperature for enough time to keep the system temperature stable. Then, we gradually decreased the superficial gas velocity to 0 and kept the bed static for 3 min before conducting calibration to obtain the high calibration value (C_H).

Silica particles were utilized in the experiments and were first precalcined at 600 °C for 4 h to stabilize their physical and chemical properties. The Sauter mean diameter of the silica particles was measured as 237 μm using a particle size analyzer (Mastersizer 3000, Malvern Instruments Ltd., UK). Figure 2 presents the size distribution and a typical scanning electron microscope (SEM) image of the silica particles. To represent the sphericity of silica particles, we used their circularity, which takes into account the similarity of length in the three-dimensional direction.[29] We detected, separated, and measured the circularity of the particles using SEM images. After analyzing 10 SEM images, the circularity of the silica particles was recorded as 0.69. The physical properties and elementary compositions of the particles were obtained with a Philips Magix-601 X-ray fluorescence spectroscope (XRF; see Table 1).

The high-temperature ECT sensor consists of eight electrodes, with its center located 185 mm above the distributor on a horizontal plane. Its main parameters are presented in Table 2; it can work up to 800 °C, and the detailed design was reported previously.[26]

Table 1. Physical Properties and Chemical Compositions of Silica Particles

parameters	value
mean diameter/μm	237
density/(kg/m^3)	2650
compositions	
Si	46.056
O	53.100
Al	0.588
K	0.124
Fe	0.056
Ca	0.035
P	0.024
Ti	0.010
Zr	0.004

Table 2. Parameters of the Experimental Apparatus

parameters	value
column inner diameter	48 mm
column thickness	2 mm
number of electrodes	8
electrode thickness	0.5 mm
electrode-to-gap ratio	4
electrode length	30 mm

Our experimental setup, as illustrated in Figure 1, only allows us to measure the total pressure drop across the fluidized bed, distributor, and preheating section. However, we need to determine the actual pressure drop of the fluidized bed, which requires separating the pressure drops of the distributor and the preheating section from the total pressure drop. To achieve this, we measured the pressure drops of the distributor and the preheating section with the empty bed in advance and subtracted them from the total pressure drop measurements at the same superficial gas velocity. We did not measure pressure drops of the empty beds at all superficial gas velocities but instead measured them across the superficial gas velocity range and fitted quadratic functions between the pressure drop of the empty bed and superficial gas velocity based on the Ergun equation. In experiments, pressure drop data were recorded in intervals of 125 Hz and for a duration of 80 s. For a given superficial gas velocity, the pressure drop of the fluidized bed was derived by subtracting the pressure drop across the empty column from the total pressure drop across the bed, as depicted by eq 2.

$$\Delta P_{\text{fluidizedbed},V} = \Delta P_{\text{total},V} - \Delta P_{\text{empty},V} \tag{2}$$

3. METHODOLOGY

After capacitance vectors are obtained during the fluidized bed measurements, the permittivity distribution according to eq 3 can be obtained through specified algorithms.[28]

$$\lambda = Sg \tag{3}$$

where λ is the normalized capacitance vector, g is the normalized permittivity, and S is the normalized sensitivity distribution. The projected Landweber iteration algorithm with an optimal step length is used to obtain the normalized permittivity distribution, and the iteration number of iterations is set to 200 according to our previous work.[30,31] The effect of

temperature on image reconstruction can be referred to in our previous work.[26]

Once the normalized permittivity distribution ($\hat{g}$) is obtained, the solid fraction distribution and time-averaged solid fraction with its standard deviation can be calculated by the following equations.

$$p = \frac{\sum_{i=1}^{N} \hat{g_i} * s_i}{\sum_{i=1}^{N} s_i} \tag{4}$$

$$\overline{p} = \frac{1}{Q} \sum_{i=1}^{Q} p_i \tag{5}$$

$$\beta = \theta \cdot p \tag{6}$$

$$\overline{\beta} = \frac{1}{Q} \sum_{i=1}^{Q} \beta_i \tag{7}$$

$$\text{STD} = \frac{1}{Q} \sum_{i=1}^{Q} ((\beta_i - \overline{\beta})^2 \tag{8}$$

where p is the average normalized permittivity of each frame, s is the area of each image pixel, N is the number of pixels (3228 in this work), $\overline{p}$ is the time-averaged normalized permittivity, Q is the number of frames (20 000 in this work), p_i is the average normalized permittivity of the ith frame, β is the average solid fraction of each frame, $\overline{\beta}$ is the time-averaged solid fraction, β_i is the average solid fraction of the ith frame, and STD is the standard deviation of $\overline{\beta}$.

A parallel model has been used to establish the correlation between the normalized permittivity and the solid fraction as shown in eq 6.[21,32] Note that θ is the average solid fraction of the packed bed, which varies with temperature because the packed bed height can expand with the increase in temperature. Previous studies have demonstrated that packed bed height increases with the rise in interparticle forces[17,18,33,34] because of the decrease in the coordination number of each particle (as discussed in a previous study[33]). To measure the packed bed height, a ruler made from a stainless-steel rod and held by a device mounted on the outlet of the fluidized bed was used. The ruler could move freely along the bed's axial direction, and the packed bed height was recorded at the surface below which particles visibly adhered to the rod.

4. RESULTS AND DISCUSSION

4.1. Visualization of Fluidization Transition. A series of measurements in the fluidized bed at different temperatures (T = 20, 200, 400, and 600 °C) were carried out using the high-temperature ECT sensor. The superficial gas velocity was increased for each temperature from 0 to 10.0 cm/s with the same stepwise increment. Before measurements for each temperature were made, the static height of the packed bed without gas flow was obtained. The average packed bed height was 23.7, 24.4, 25.3, and 26.6 cm for T = 20, 200, 400, and 600 °C, and the corresponding average solid fractions are listed in Table 3.

Figure 3 shows the typical solid fraction distributions measured by the high-temperature ECT sensor. We obtained the solid fraction distribution by the projected Landweber iteration algorithm with an optimal step length. As shown in the figure, when the superficial gas velocity gradually increases, the appearance of bubbles can be distinguished, allowing for

**Table 3. Average Packed Bed Height and Solid Fraction at Different Temperatures**

temperature (°C)	average packed bed height (cm)	average solid fraction
20	23.7	0.53
200	24.4	0.52
400	25.3	0.50
600	26.6	0.47

the identification of the transition to bubbling fluidization at different temperatures. A closer inspection of the solid fraction distribution snapshots taken at different temperatures reveals that the first bubble appears at a superficial gas velocity of 4.8, 4.0, 3.7, and 3.5 cm/s for $T = 20$, 200, 400, and 600 °C, respectively.

4.2. Minimum Bubbling Velocity (U_{mb}). It is widely accepted that the minimum bubbling velocity (U_{mb}) is the superficial gas velocity at which bubbles regularly occur.[8,35−37] We can distinguish the occurrence of bubbles in a three-dimensional fluidized bed via ECT images, with U_{mb} values of 4.8, 4.0, 3.7, and 3.5 cm/s observed for $T = 20$, 200, and 600 °C, respectively. To verify the observed results, the time series of solid fractions obtained via the ECT measurement was further analyzed. This analysis revealed regular fluctuations in the solid fraction, as seen in Figure 4. These fluctuations were caused by the regular occurrence of bubbles, which were used to plot the variations of the time-averaged solid fraction and its standard deviation against superficial velocity (seen in Figure 5). This allowed for the determination of the minimum bubbling velocity, which was indicated by the jump point representing regular bubbles passing through the sensor (bed). This figure demonstrates that an obvious jump point exists in the curve of time-averaged solid fraction standard deviation versus superficial gas velocity at different temperatures, representing regular bubbles passing through the sensor (bed). These results provide evidence of the minimum bubbling velocity at different temperatures.

The pressure drop of the bed against superficial gas velocity curves can also be used to determine U_{mb} according to Rapagnà et al.,[38] as shown in Figure 6, where U_{mb} is determined by a shallow minimum. The minimum bubbling velocity U_{mb} obtained from the pressure-drop against superficial gas velocity curves is 4.8 cm/s for $T = 20$ °C, 4.0 cm/s for $T = 200$ °C, 3.7 cm/s for $T = 400$ °C, and 3.5 cm/s for $T = 600$ °C. These results confirm the reliability of high-temperature ECT in measuring the minimum bubbling point in fluidized beds. In conclusion, high-temperature ECT can provide a direct and accurate way to determine the minimum bubbling velocity from the reconstructed images of the solid fraction distribution of a fluidized bed.

4.3. Minimum Fluidization Velocity (U_{mf}). Under ambient conditions, silica particles used in our experiments are typically Geldart B particles, meaning that their minimum bubbling velocity (U_{mb}) and minimum fluidization velocity (U_{mf}) should be the same. To determine minimum fluidization velocity (U_{mf}), we used a method based on measuring the pressure drops across the fluidized bed against superficial gas velocity during the defluidization process. Specifically, we employed the method described by Rao et al.,[39] where the intersection of the extrapolated line of the pressure drops across the packed bed and that of the total pressure drop across the fully fluidized bed is used to indicate the minimum fluidization point. As shown in Figure 6, we obtained $U_{mf} = 4.80$, 3.61, 3.20, and 2.89 cm/s for temperatures of 20, 200, 400, and 600 °C, respectively, based on the pressure drop against superficial gas velocity curves. Apparently, under the ambient conditions ($T = 20$ °C), U_{mf} and U_{mb} are coincident. It is noteworthy that pressure-drop hysteresis became more pronounced with increasing temperature, leading to a non-linear decrease in pressure drop near the minimum fluidization velocity and creating the difference between the fitting line at room temperature and those at elevated temperatures.
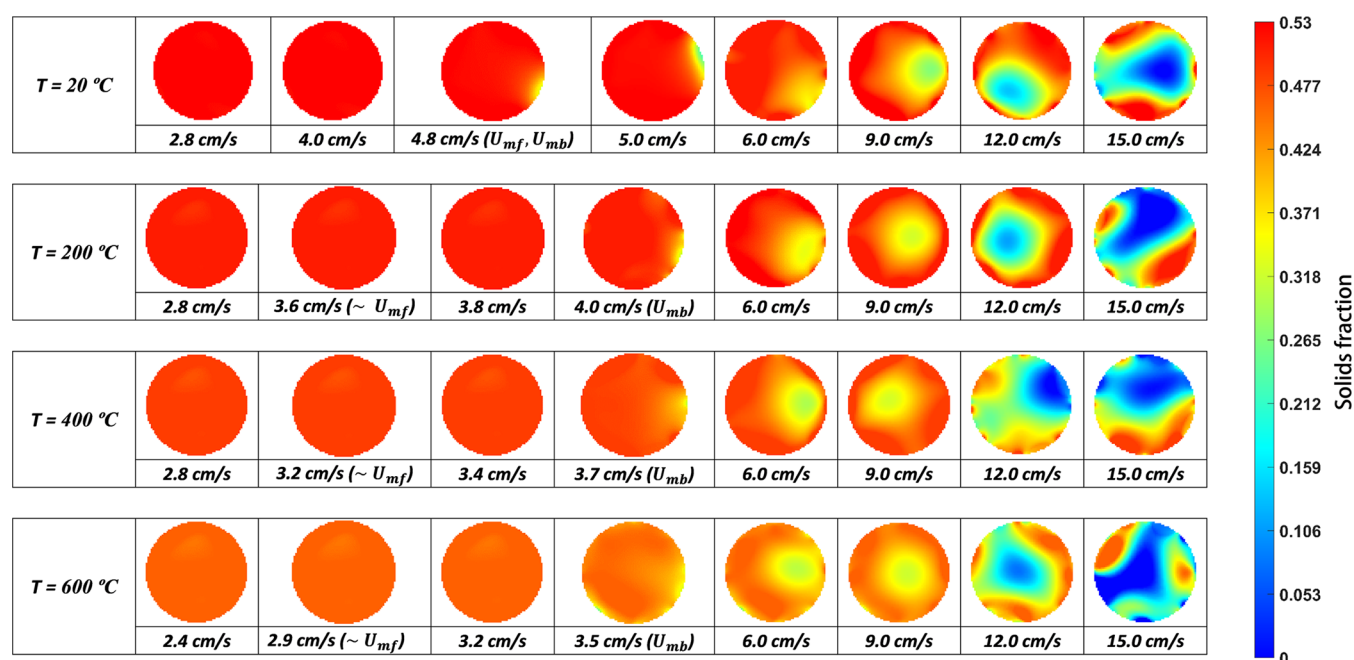
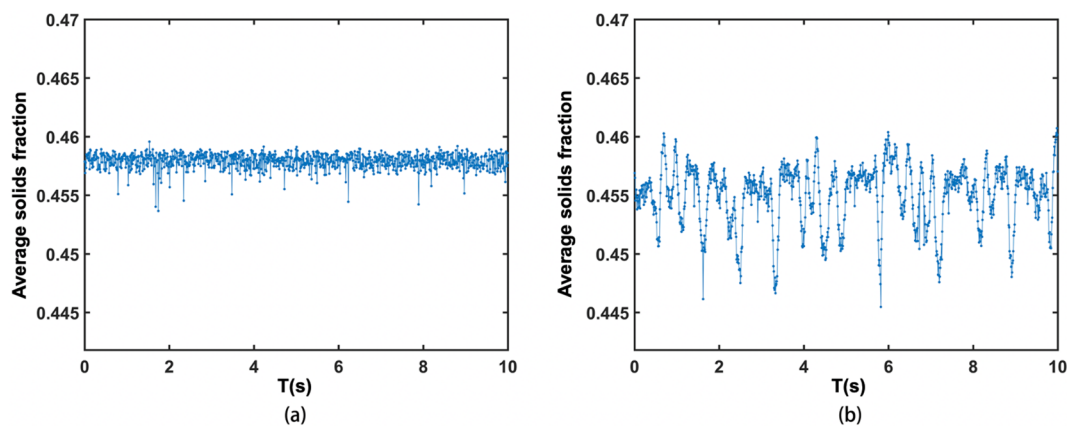**Figure 3.** Snapshots of solid fraction distribution at different temperatures.

Figure 4. Time series of solid fractions at different superficial gas velocities, (a) V = 2.8 cm/s and (b) V = 2.9 cm/s (U_{mb}).
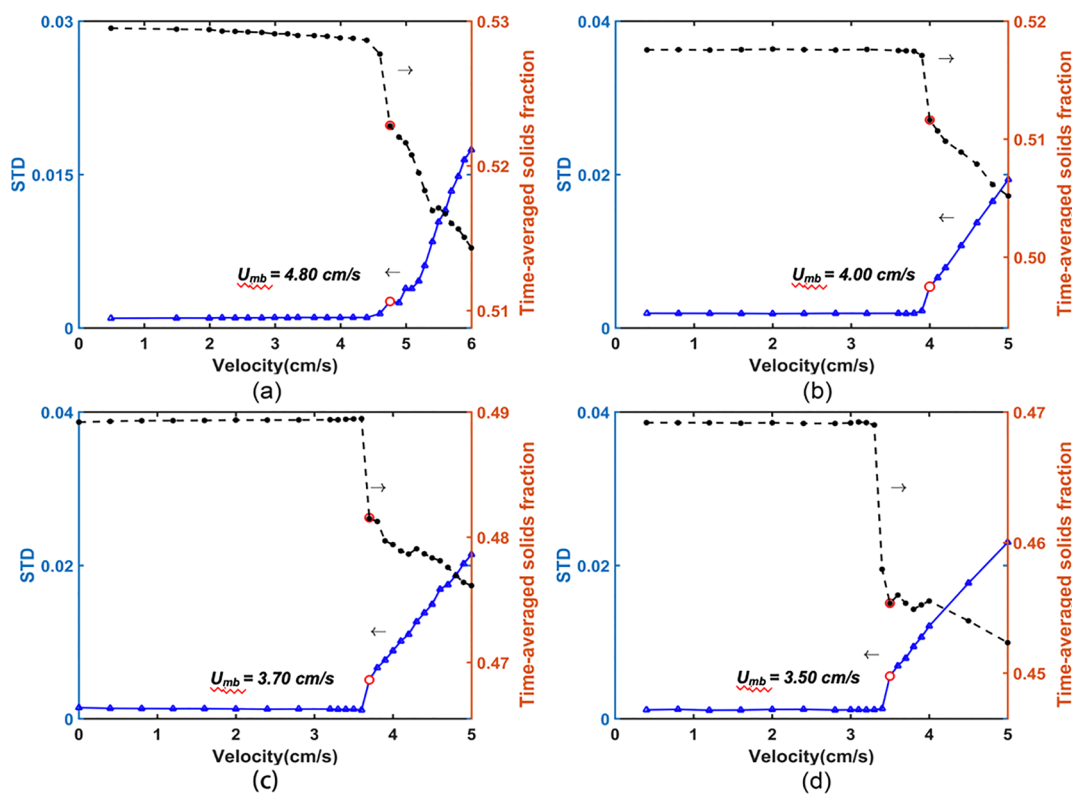

Figure 5. Variation of the time-averaged solid fraction and its standard deviation with the superficial gas velocity at different temperatures: (a) 20 °C, (b) 200 °C, (c) 400 °C, and (d) 600 °C.

The U_{mf} is then compared with an empirical correlation, as shown in eq 9, which accurately predicts U_{mf} for Geldart B particles, even at high temperatures.[40]

$$\frac{1.75}{\varnothing \varepsilon_{mf}^3} Re_{mf}^2 + 150 \frac{1 - \varepsilon_{mf}}{\varnothing^2 \varepsilon_{mf}^3} Re_{mf} = Ar \tag{9}$$

where the Reynolds number and Archimedes numbers are respectively defined as

$$Re_{mf} = \frac{d_p \rho_g U_{mf}}{\mu} \tag{10}$$

$$Ar = \frac{d_p^3 \rho_g (\rho_p - \rho_g) g}{\mu^2} \tag{11}$$

Note that $\varnothing$ is the sphericity of particles, ε_{mf} is the void fraction at minimum fluidization, ρ_p is the particle density, ρ_g is the gas density, d_p is the Sauter mean diameter of particles, μ is the gas viscosity, and g is the gravitational constant. Based on the measurements of changes in average solid fraction against superficial gas velocity (shown in Figure 5), it is evident that the void fraction remains stable before the bubbling regime. This ensures that the minimum fluidization voidage (ε_{mf}) equals the voidage in the packed bed regime (as displayed in Table 3).

According to the Ergun eq 9, when the Reynolds number is smaller than 1, the viscous effect is dominant.[40] The Reynolds numbers for T = 20, 200, 400, and 600 °C are 0.75, 0.25, 0.12, and 0.07, respectively, thus, eq 9 can be simplified to eq 12, where the second term is negligible.
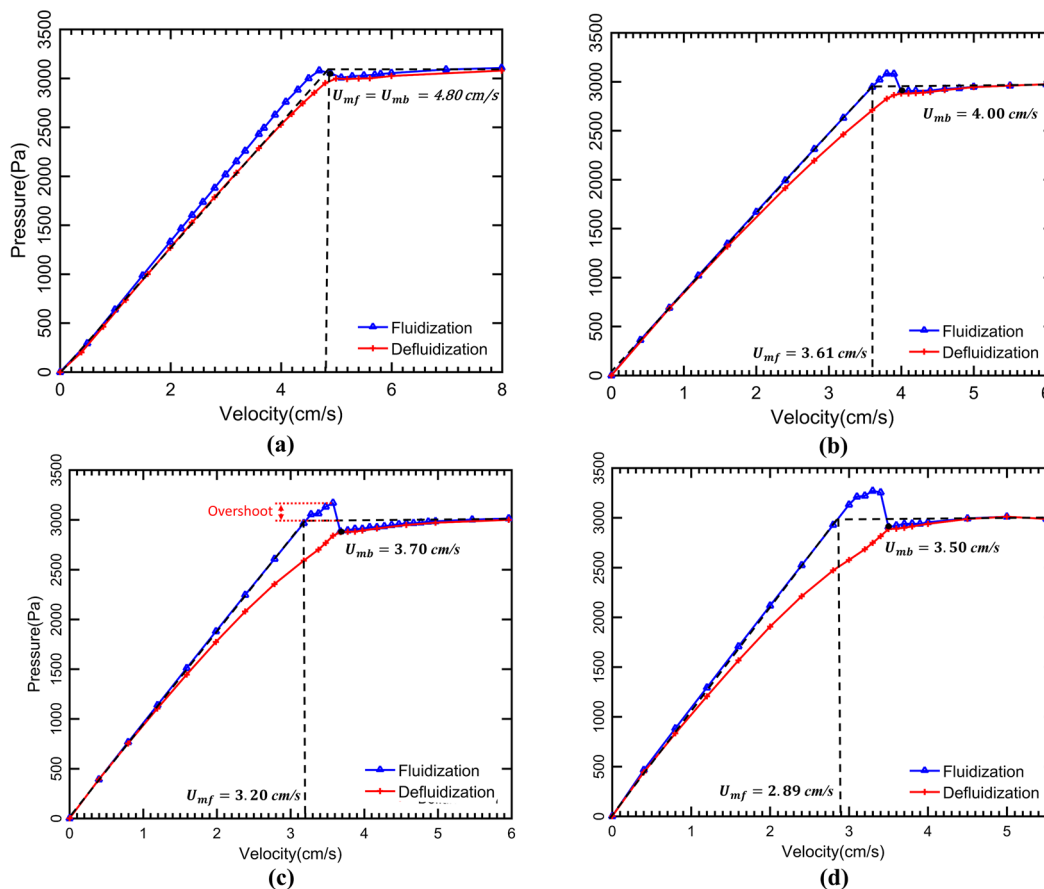
Figure 6. Pressure drop across the fluidized bed against superficial gas velocity at (a) $T = 20\ °C$, (b) $T = 200\ °C$, (c) $T = 400\ °C$, and (d) $T = 600\ °C$.

$$U_{mf} = \frac{d_p^2(\rho_p - \rho_g)g\phi^2\varepsilon_{mf}^3}{\mu(1 - \varepsilon_{mf})} \tag{12}$$

By simplifying eq 12 in eq 13, where $K = d_p^2(\rho_p - \rho_g)g\phi^2$, we obtain

$$U_{mf} = K\frac{\varepsilon_{mf}^3}{\mu(1 - \varepsilon_{mf})} \tag{13}$$

The Wen−Yu equation,[41] presented in eq 14, is applicable to high-temperature systems by Pattipati and Wen.[42] Thus, the Wen and Yu equation was also utilized to predict the U_{mf} for comparison purposes, although it assumes minimum fluidization voidage (ε_{mf}) is only related to sphericity.

$$Re_{mf} = \sqrt{(33.7^2 + 0.0408Ar)} - 33.7 \tag{14}$$

Figure 7 compares the measured U_{mf} with the predicted U_{mf} via eq 9 and eq 14. As can be seen, at lower operating temperatures ($T = 20$ and $200\ °C$), the measured U_{mf} agrees well with both predictions; however, as the temperature rises, the differences between the predictions and measurements become more pronounced. According to the Ergun equation, at a low Reynolds number (<1), the dominant effect is viscous, which causes a decrease in U_{mf} supporting invariable of minimum fluidization voidage (ε_{mf}), yet the measured values are higher than the values predicted by the Wen and Yu equation, indicating that interparticle forces partially counterbalance the viscous effect and heighten U_{mf} at high temperatures. Consequently, the Wen and Yu correlation
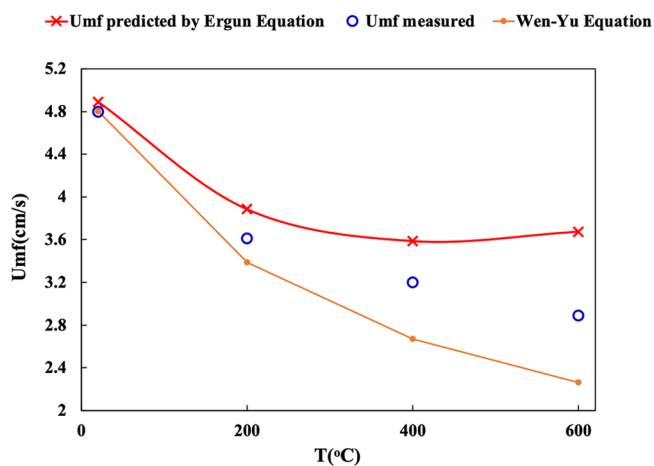

Figure 7. Comparisons of U_{mf} obtained from measurements and predictions based on the Ergun equation (eq 9) and the Wen−Yu correlation (eq 14) for different temperatures.

demonstrated the impact of temperature-induced interparticle forces on the fluidization bed behavior. Moreover, we also found that the measured results are smaller than the values predicted by eq 9 directly according to the Ergun equation. As illustrated above, at low Reynolds, eq 9 is simplified to eq 12. As illustrated in eq 12, voidage at the minimum fluidization state and viscosity of air increase with the temperature, which have opposite effects on U_{mf} and illustrates the variation trend of U_{mf} in Figure 7. As a result, the calculated results are higher

than the measured results owing to the increase in minimum fluidization voidage. The increase in minimum fluidization voidage causes the real velocity in the packed bed to decrease when setting the same superficial gas velocity. When this role is greater than the role of interparticle forces, we can determine that the calculated results are higher than the predictions at high temperatures. Therefore, it can be argued that the change in interparticle forces leads to different variation trends at elevated temperatures.

It is noteworthy that bed height has an effect on fluidization characteristics, including minimum fluidization velocity and gas holdup values.[43,44] In our study, we used the same mass of silica particles at different temperatures, resulting in a variation in packed bed height due to the temperature effect on the packed bed voidage. According to our measurements, the packed bed heights at 20 °C, 200 °C, 400 °C, and 600 °C were 23.7, 24.4, 25.3, and 26.6 cm, respectively, with variations of 3.0%, 6.7%, and 12.2% compared to the packed bed height at 20 °C. Korkerd et al. studied the impact of bed height on minimum fluidization velocity using a 10.2 cm inner diameter bed and three different diameters of silica particles.[43] They obtained that the change in minimum fluidization velocity is proportional to the variation of $(H_0/D_0)^{0.076}$, where H_0 is packed bed height and D_0 is bed diameter. Thus, when we assumed the bed heights at elevated temperatures were the same as that at room temperature, the deviations of minimum fluidization velocity (U_{mf}) were estimated to be 0.2%, 0.5%, and 0.9%, representing that the change in bed height has no effect on minimum fluidization velocities. Escudero and Heindel also conducted an investigation into the effect of bed height on fluidized bed characteristics, including minimum fluidization velocity and gas holdup.[44] They utilized pressure drop and X-ray computed tomography measurements to examine bed height's effects on the above parameters through three different Geldart B particles (glass beads, ground walnut shell, and ground corncob) in a 10.2 cm diameter fluidized bed. Their results indicated that bed height had no effect on minimum fluidization velocity and local time-average gas holdup values. Consequently, we can believe that the minor change in bed height induced by temperature would have no effect on the fluidization characteristics in this study.

4.4. Fluidization Behavior Transition from Geldart B to A. According to Geldart, fluidization of Geldart B and A particles has typical features as follows:[8]

Group B: Bubbles occur when the bed commences fluidization, which is featured by $U_{mf}/U_{mb} = 1$.

Group A: A homogeneous fluidization regime, in which no bubble appears between U_{mf} and U_{mb}, leading to $U_{mb}/U_{mf} > 1$.

Based on the above measurement results, Figure 8 shows that U_{mb}/U_{mf} is 1 under ambient conditions ($T = 20$ °C), indicating Geldart B fluidization behavior. When the temperature increases to 200 °C, homogeneous fluidization between U_{mf} and $1.108U_{mf}$ is observed, typical of Geldart A fluidization behavior. Further, increases in temperature to 400 and 600 °C result in an enlarged interval of homogeneous fluidization from $1.156U_{mf}$ to $1.211U_{mf}$. This suggests that the fluidization behavior transits from Geldart B to A type when the operating temperature increases from ambient to 600 °C.

To better understand the mechanism behind the transition in the fluidization behavior of silica particles in this study, we studied the pressure overshoot at the onset of fluidization, which is closely related to the cohesive interparticle forces.[13,18,19,33] Figure 9 shows the pressure overshoot, which
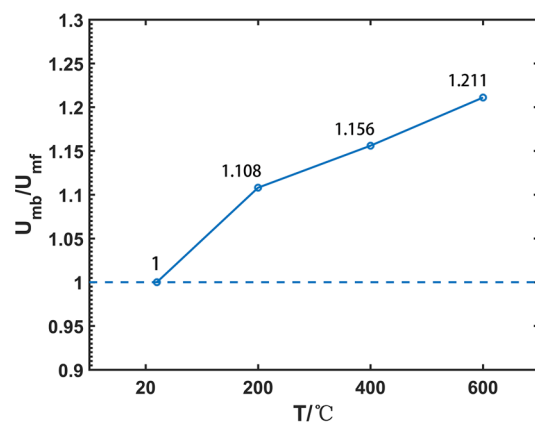

Figure 8. Ratio of U_{mb}/U_{mf} at different temperatures.
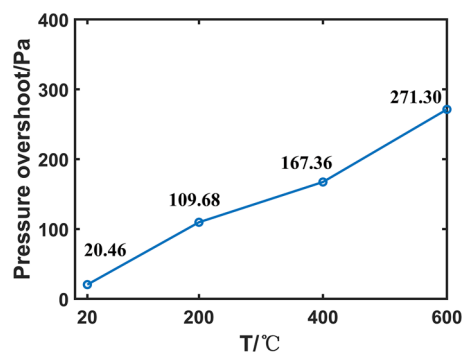

Figure 9. Pressure overshoots of the fluidized bed at different temperatures.

is obtained by subtracting the fluidized bed pressure drop from the maximum pressure drop over the superficial gas velocity curve, as indicated in Figure 6. The pressure overshoot becomes higher with the increase in temperature, suggesting that the cohesive interparticle forces are enhanced with the increase in temperature.[19] Therefore, the transition in silica particle fluidization behavior from Geldart B to A at elevated temperatures is mainly due to the increased cohesive interparticle forces. The increase in interparticle forces may be due to the compositions of elements. According to Table 1, the silica particles are mainly composed of Si and O, with minor amounts of Al and K. Previous research has found that alkali metal elements in silica particles can lead to the formation of silicates, which have low-melting points, such as $K_2O \cdot SiO_2 = 976$ °C, $K_2O \cdot 2SiO_2 = 1015$ °C, $K_2O \cdot 3SiO_2 = 740$ °C, and $K_2O \cdot 4SiO_2 = 764$ °C.[33,45] These low melting points can soften particles and increase interparticle forces at elevated temperatures. Further studies are being conducted in order to validate the hypothesis.

Castellanos et al.[46] found that the overshoot pressure ΔP_t can be directly related to the tensile yield strength σ_t of particles via

$$\sigma_t = \Delta P_t \tag{15}$$

The tensile yield strength σ_t can be further used to estimate the cohesive interparticle forces (F_c) following Molerus.[47]

$$F_c = \frac{d_p^2 \sigma_t \pi}{k \cdot (1 - \varepsilon_{mf})} \tag{16}$$
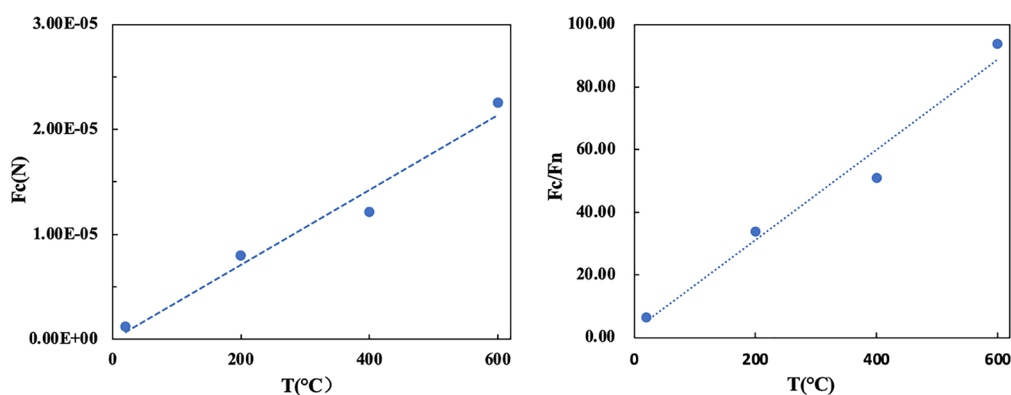
Figure 10. Variations in (a) cohesive interparticle forces (F_C) and (b) the ratio of cohesive interparticle forces to hydrodynamic forces (F_C/F_N) against temperatures of silica particles at the incipient fluidization state.

Here, k is the coordinate number and can be estimated by the bed voidage,[48] as shown in eq 17:

$$k = 17.517 - 41.838\varepsilon + 37.082\varepsilon^2 - 10.815\varepsilon^3 \quad (17)$$

By eq 16, the cohesive interparticle forces at the incipient fluidization can be estimated. The estimated forces show an almost linear increase with temperature (see Figure 10a). The Bond number (B_O)—the ratio of cohesive interparticle forces to particle weight—is 7.19, 43.74, 66.77, and 124.17 for $T = $ 20, 200, 400, and 600 °C, respectively. This is consistent with the results of Valverde and Castellanos,[49] which observed a transition from Geldart C to A in a modified 8.53 μm xerographic toner with a B_O of 550. Hydrodynamic forces (F_N) at the incipient fluidization can be evaluated via eq 18, which is obtained from the equality between bed gravity force, hydrodynamic forces, and buoyancy force.[50]

$$F_N = \frac{1}{6}\pi d_p^3 (\rho_p - \rho_f) g \quad (18)$$

Figure 10b shows that the ratio of cohesive interparticle forces (F_C) to hydrodynamic forces (F_N) increases with temperature. F_C/F_N rises from 5.60 at 20 °C to 93.8 at 600 °C. As illustrated by Mostoufi,[10] the variation in F_C/F_N represents the transition in fluidization behaviors, which is also consistent with the variation of U_{mb}/U_{mf}, indicating that the variation of U_{mb}/U_{mf} is closely related to that of F_C/F_N.

The elevated temperature affects the fluidization behavior via two aspects. On the one hand, it changes the gas properties, such as gas density and viscosity, which influences the hydrodynamic interaction between particles and gas. On the other hand, it alters the surface property of particles, leading to variation in cohesive interparticle forces. Based on the discussion, it can be concluded that, at low temperatures, the change in gas properties due to the elevated temperature is primarily responsible for the fluidization behavior. At high temperatures, however, the change in cohesive interparticle forces caused by the alteration of surface properties becomes influential. In summary, both facets contribute to the transition of the fluidization behavior from Geldart B to A. Therefore, it can be seen that our findings are consistent with those works obtained by pressure drop measurements, including the increase in minimum fluidization void fraction,[11,12] and the fluidization transition is also due to the increase in interparticle forces,[13,15] thus showing the temperature effect on fluidization characteristics changes.

4.5. Bed Expansion Characteristic in Homogeneous Regime. The ECT measurement allows us to obtain a series of solid fractions at different superficial gas velocities. Therefore, we can calculate the bed expansion by observing the variation of time-averaged solid fractions with respect to superficial gas velocity.[23] Figure 5 shows the variation of time-averaged solid fraction, as well as its standard deviation, against the superficial gas velocity. The horizontal ordinates of red circles are equal to the minimum bubbling velocities at different temperatures. The figure shows that the time-averaged solid fraction starts decreasing around the minimum bubbling velocity. This decrease occurs at 20, 200, and 400 °C at the minimum bubbling velocity. At 600 °C, however, the time-averaged solid fraction starts decreasing when the superficial gas velocity is 0.1 cm/s lower than the minimum bubbling velocity, indicating the adjustment of bed structure around the minimum bubbling velocity.

We can verify that the temperature effect causes a transition in the fluidization behavior of silica particles from Geldart B to A. However, the bed expansion behavior observed in the homogeneous regime is different from that of conventional Geldart A particles when the transition occurs. In the homogeneous fluidization regime of the traditional Geldart A particles, the bed expansion behavior can be described by the Richardson and Zaki equation.[51,52] This phenomenon is also captured in this work by using ECT to measure FCC particles, which belong to Geldart A particles at 600 °C.

Figure 11 shows the variation of time-averaged solid fraction and its standard deviation of FCC particles against superficial gas velocity at 600 °C. From the figure, it is easy to obtain minimum fluidization velocity and minimum bubbling velocity from the curve of time-averaged solid fraction against superficial gas velocity. When the fluidized bed starts fluidizing, the bed expands, causing the time-averaged solid fraction to decrease. This superficial gas velocity represents the minimum fluidization velocity. Additionally, the standard deviation of the time-averaged solid fraction is slightly varied when the bed begins fluidizing, which represents a stable state of the fluidized bed. With the increase in superficial gas velocity, the fluidized bed continuously expands until the bed enters the bubbling regime, resulting in a reversal of changes in the time-averaged solid fraction due to bubble formation and passage through the bed. At the same time, the formation and movement of bubbles also induce a violent fluctuation of the standard deviation of the time-averaged solid fraction. It is found that in the homogeneous fluidization regime, the time-averaged solid
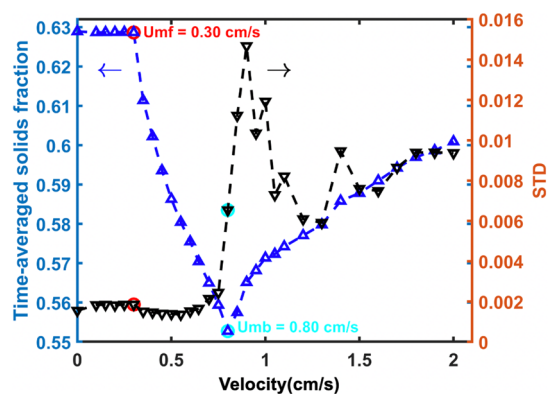
Figure 11. Variations of average solid fraction and its standard deviation of FCC particles against superficial gas velocity at 600 °C.

fraction decreases noticeably with the superficial gas velocity. The variation in time-averaged solid fraction ranges from 0.63 to 0.55 when crossing the homogeneous regime, equaling a 13% variation ratio. However, when silica particles are fluidized at high temperatures, the time-averaged solid fraction's variation with respect to superficial gas velocity reflects different fluidization characteristics. From Figure 5, it is determined that the variation ratio of the time-averaged solid fraction is only 1.11%, 1.50%, and 3.00% at the temperatures of 200, 400, and 600 °C, respectively, when the bed changes from the packed bed to the bubbling regime. This indicates that the fluidized bed does not expand until superficial gas velocity surpasses the minimum bubbling velocity. This fluidization characteristic differs from the traditional Geldart A particles, such as FCC particles, which expands once their superficial gas velocity meets the minimum fluidization velocity. The difference in behavior between Geldart A particles (e.g., FCC particles) and silica particles can be attributed to their different

properties, such as diameter, density, porous structure, and surface properties, which need further investigation. Also, this was first measured with a high-temperature ECT sensor and should be taken into consideration when performing high-temperature fluidization processes.

4.6. Bubble Characteristics. The characteristics of bubbles are essential for the performance of gas–solids fluidized beds. Compared to other techniques, ECT can measure the solid fraction distribution, allowing us to measure bubble and emulsion phases.

Based on previous studies, the ability to produce small size and multiple numbers of bubbles is also a clear characteristic of Geldart A.[8] As described in our previous study,[26] using ECT measurements, we were able to measure the characteristics of the fluidized bed based on the analysis of time series of average solid fractions (as displayed in Figure 4). The periodic variation of bubbles passing through the sensor indicates that the dominant frequency obtained from the frequency domain analysis of the time series of the average solid fraction can represent the bubble behavior.[25] Based on this method, we can distinguish between the single-bubble and multibubble regimes. The single-bubble regime complies with a dominant frequency indicating the bubble passing; however, there is no such frequency in the multibubble regime as the motions of multiple bubbles are complex. Thus, we compared the spectrum distribution of the time series of average solid fractions in order to detect if the bubble pattern of the initial bubbling state changes with increasing temperature.

Figure 12 shows the spectrum distributions at velocities that were 0.3 cm/s higher than the minimum bubbling velocities and different temperatures. By comparing results from slightly bigger velocities than the minimum bubbling velocity, we can observe that the fluidization state does not alter with increasing temperature, and a single bubble with a frequency of
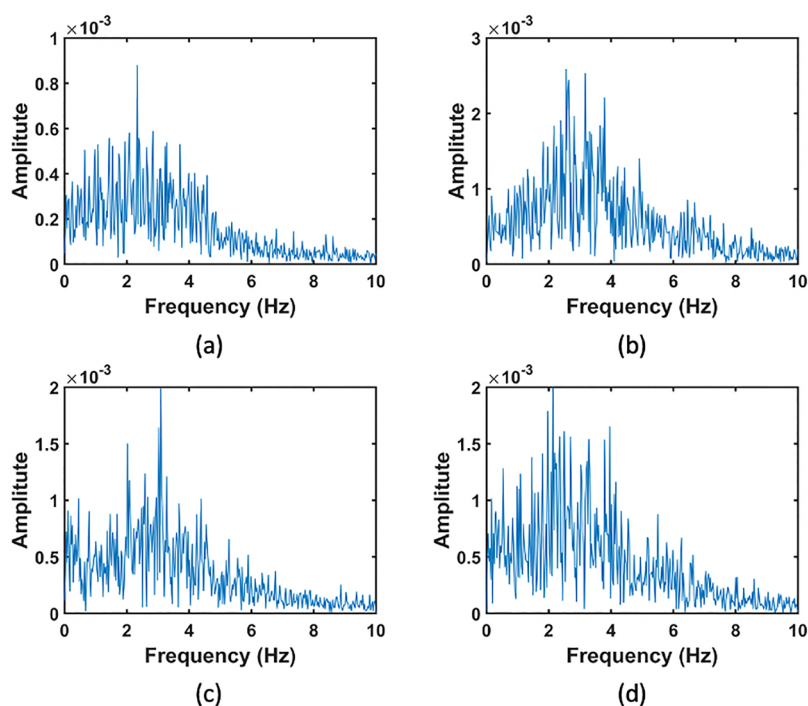

Figure 12. Spectrum distributions at velocities that are 0.3 cm/s bigger than the minimum bubbling velocities and different temperatures, (a) 20 °C, (b) 200 °C, (c) 400 °C, (d) 600 °C.

approximately 3 Hz is more likely to pass through the sensor. This is also distinct from that of traditional Geldart A particles such as FCC particles, which more often form multiple bubbles at the beginning of bubbling. The spectrum distributions of FCC particles nearby the minimum bubbling velocity are also displayed in Figure 13. There is no dominant frequency, and noise is predominant.
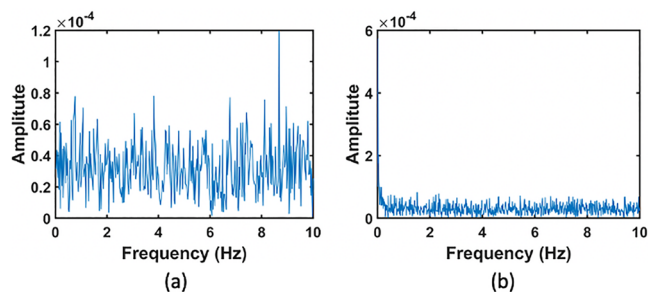
Figure 13. Spectrum distributions of FCC particles at (a) 0.1 cm/s higher and (b) 0.2 cm/s higher than minimum bubbling velocity states, 600 °C.

Next, we discussed the variation in bubble size. We followed Agu et al.'s approach and used a fast frequency capacitance acquisition system (around 115 Hz) to measure average bubble sizes.[53] The process of computing bubble size starts with identifying whether the bubble is located in the middle plane of the sensor. This is accomplished by assessing the time series of the average solid fraction, when the measured value is equal to the valley level, as shown in Figure 4; further details can be found in our previous study.[31] Afterward, the same threshold (i.e., 0.3) is employed to differentiate between the bubble and emulsion phases. We then computed the equivalent bubble diameter assuming a spherical bubble using eq 19.

$$d_b = \frac{1}{n}\sqrt{\frac{4A_{b,i}}{\pi}} \tag{19}$$

Here, n is the number of individual bubbles and $A_{b,i}$ is the projected area when the bubble is located in the middle of the ECT sensor. The formula to compute the projected area ($A_{b,i}$) is shown in eq 20:

$$A_b = A\left(\frac{N_b}{N_{pix}}\right) \tag{20}$$

where A is the cross-sectional area of the bed and N_b is the number of pixels occupied by bubbles after binarizing the normalized permittivity distribution into bubble and emulsion phases. A more detailed explanation of the process for computing average bubble diameter can be found in prior studies.[31,53]

Figure 14a shows the change in average bubble diameter with temperature over a range of superficial gas velocities, which range from $1.71U_{mb}$ to $4.29U_{mb}$ for 600 °C experiments. Fast Fourier transform of the time series of the average solid fraction can be used to identify a dominant frequency that has the maximum module in the frequency domain. This dominant frequency can represent the frequency of bubbles passing through the sensor. Figure 14b shows the variation of dominant frequency with temperature over the same range of superficial gas velocities. Figure 14a shows that the average bubble diameter increases with both increased superficial velocity and increased temperature at the same superficial gas velocity. From Figure 14b, it is seen that the dominant frequencies decrease with increasing superficial velocity but are not influenced by temperature. Considering a similar dominant frequency at the same superficial gas velocity and different temperatures, it can be concluded that the bubble phase increases with temperature, leading to a reduction in fluidization quality with an increase in temperature. In addition, we also computed the average bubble diameter of FCC particles at different temperatures and relative superficial gas velocities within a range of $2.5U_{mb}$ to $8.75U_{mb}$ for the 600 °C experiments. As shown in Figure 15, there is an inverse trend between the average bubble diameter and temperature; the average bubble diameter decreases with an increase in temperature. The cause for this is discussed below.

We computed the variation of interparticle forces (F_c) and interparticle forces/hydrodynamic forces (F_c/F_N) of FCC particles against temperature in the incipient fluidization state based on eq 16 and eq 18, respectively. The results are presented in Figure 16, which is different from the silica particle behavior. Bubble size is related to the ratio of hydrodynamic forces (F_N) to interparticle forces (F_c).[15,54] Our results indicate that the bubble size of silica particles increases
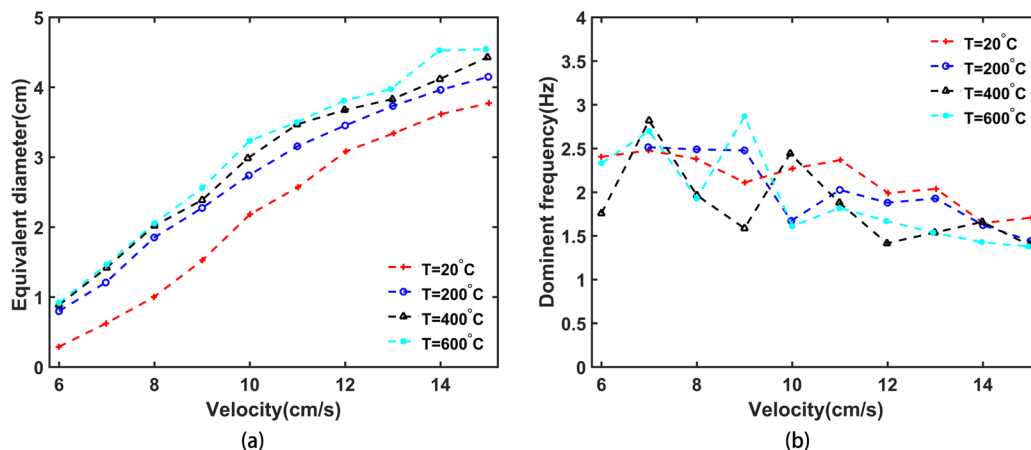
Figure 14. Variation of (a) average bubble diameter and (b) dominant frequency of silica particles with superficial gas velocities at different temperatures.
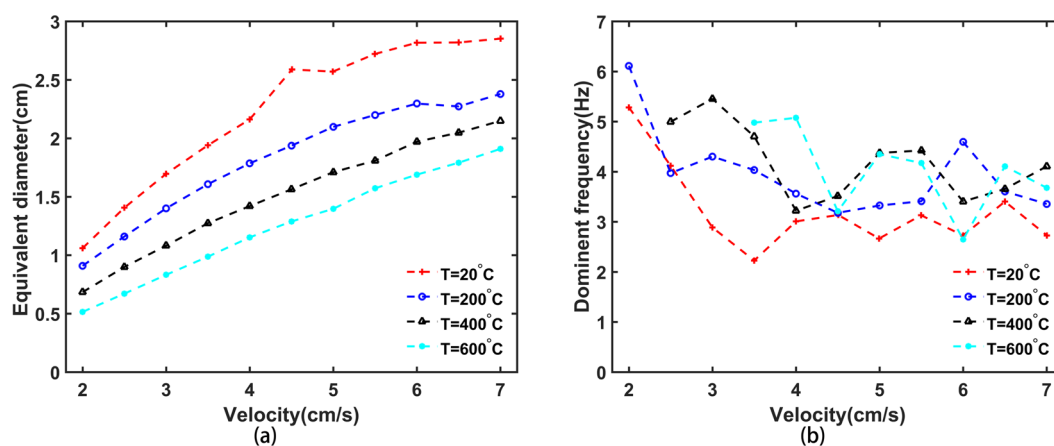
Figure 15. Variation of (a) average bubble diameter and (b) dominant frequency with the superficial gas velocity at different temperatures for FCC particles.
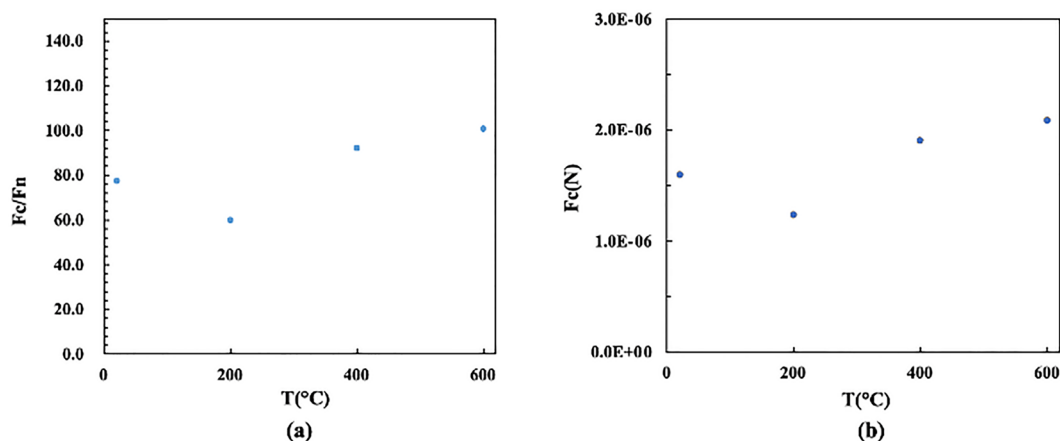

Figure 16. Cohesive interparticle forces induced by high temperatures: (a) cohesive interparticle force F_C and (b) F_C/F_N of FCC particles at the incipient fluidization state.

with temperature, while F_c/F_N also increases as the temperature increases in the incipient fluidization state. This result is in agreement with the findings of Ma et al.[55] On the other hand, the bubble size of FCC particles decreases with rising temperature, and the temperature has little effect on F_c/F_N in the initial fluidization stage. It should be noted that F_N is estimated by the net gravitational force as eq 18. For FCC particles, the interparticle forces are not sensitive to temperature (seen in Figure 16a), whereas the hydrodynamic forces increase with temperature due to the increase in gas viscosity at the same superficial gas velocity.[56] The interparticle forces of silica particles increase with temperature (as indicated in Figure 10a), and the hydrodynamic forces of silica particles decrease with temperature since the inertia effect plays a major role for coarse particles at the same superficial gas velocity.[56] Therefore, F_c/F_N decreases for FCC particles but increases for silica particles when the temperature increases at the same superficial gas velocity.

From the measurements discussed, two different trends of bubble equivalent diameter variation with temperature were observed, which reflects the different variation trends of F_c/F_N of silica particles and FCC particles. This indicates that fluidization quality is dependent on F_c/F_N and is not necessarily improved with an increase in temperature. The measurement results thus validate the summary by Yates.[57]

5. CONCLUSIONS

In our research, we discovered that the fluidization behavior of silica particles, which typically exhibit Geldart B particle fluidization characteristics at ambient temperature, transitions to Geldart A particle behavior at elevated temperatures with the use of a developed high-temperature ECT sensor. Our research also indicated that the homogeneous fluidization regime of silica particles exposed to high temperatures can be visualized by ECT; however, the analysis of the time-averaged solid fraction against the superficial gas velocity curve indicates that the fluidized bed does not expand in the homogeneous fluidization regime as is the case with traditional Geldart A particles like FCC particles. In the initial bubbling state, the bed is also typically characterized by a single bubble going through, rather than multiple bubbles, which is also unlike the behavior of traditional Geldart A particles. The bubble size variation of silica particles was also monitored using ECT, which showed that their size increases with temperature while that of FCC particles decreases due to the different change trends of cohesive interparticle forces (F_c) and hydrodynamic forces (F_N) with temperature. Our results showed that elevated temperature has an effect on the fluidization behavior in a fluidized bed via two aspects: (1) changing the properties of the gas, such as its density and viscosity, and (2) altering the surface property of particles, which then affects the cohesive interparticle forces between them. At lower temperatures, the

effect of the interparticle forces is minor, and the change in the gas properties due to an increase in temperature is more important. However, at higher temperatures, the enhanced cohesive forces caused by the modification of the particle surfaces become much more influential. Both aspects work together to make a complex yet coupled contribution to the transition from Geldart B to A and to the different bed expansion characteristics at high temperatures for silica particles. Our results also show that the high-temperature ECT is potentially effective and can be used to measure fluidized beds under real industrial operation conditions.

■ AUTHOR INFORMATION

Corresponding Author

    Mao Ye − *Dalian National Laboratory for Clean Energy and National Engineering Laboratory for MTO, Dalian Institute of Chemical Physics, Chinese Academy of Sciences, Dalian 116023 Liaoning, China;* ◉ orcid.org/0000-0002-7078-2402; Email: maoye@dicp.ac.cn

Authors

    Kai Huang − *Dalian National Laboratory for Clean Energy and National Engineering Laboratory for MTO, Dalian Institute of Chemical Physics, Chinese Academy of Sciences, Dalian 116023 Liaoning, China; University of Chinese Academy of Sciences, Beijing 100049, Beijing, China;* Present Address: Key Laboratory for Green Chemical Technology of Ministry of Education, School of Chemical Engineering and Technology, Collaborative Innovation Center of Chemical Science and Engineering, Tianjin University, Tianjin 300072, Tianjin, China

    Shuanghe Meng − *Dalian National Laboratory for Clean Energy and National Engineering Laboratory for MTO, Dalian Institute of Chemical Physics, Chinese Academy of Sciences, Dalian 116023 Liaoning, China*

    Tao Zhang − *Dalian National Laboratory for Clean Energy and National Engineering Laboratory for MTO, Dalian Institute of Chemical Physics, Chinese Academy of Sciences, Dalian 116023 Liaoning, China*

    Wuqiang Yang − *Department of Electrical and Electronic Engineering, The University of Manchester, Manchester M13 9PL, United Kingdom*

    Zhongmin Liu − *Dalian National Laboratory for Clean Energy and National Engineering Laboratory for MTO, Dalian Institute of Chemical Physics, Chinese Academy of Sciences, Dalian 116023 Liaoning, China;* ◉ orcid.org/0000-0002-7999-2940

Complete contact information is available at:
https://pubs.acs.org/10.1021/acs.iecr.3c00476

Author Contributions

The manuscript was written through the contributions of all authors. All authors have given approval for the final version of the manuscript.

Notes

The authors declare no competing financial interest.

■ ACKNOWLEDGMENTS

■ NOMENCLATURE

ΔP = Pressure drop, Pa
C = Capacitance vector
S = Normalized sensitivity matrix
g = Normalized permittivity vector
N = Number of pixels in measurement zone, 3228
e = Error vector
P = Function operator
p = Average normalized permittivity of each frame
s = Pixel area
Q = Number of frames of each measurement, 20,000
STD = Standard deviation of the time-averaged solid fraction
U_{mb} = Minimum bubbling velocity, cm/s
U_{mf} = Minimum fluidization velocity, cm/s
Re_{mf} = Reynolds number at incipient fluidization
d_p = Sauter diameter of silica particles, μm
Ar = Archimedes number
ΔP_t = Pressure overshoot, Pa
F_c = Cohesive interparticle forces, N
F_N = Hydrodynamic force, N

Greek Symbols

$\varnothing$ = Sphericity
λ = Normalized capacitance vector
α = Optimal step length
β = Average solid fraction of a frame
θ = Average solid fraction of a packed bed
ε_{mf} = Void fraction at incipient fluidization
ρ_g = Air density, g/cm^3
μ = Gas viscosity, Pa·s
ρ_p = Silica density, g/cm^3
σ_t = Tensile yield strength, Pa

Superscript

$\hat{X}$ = Reconstructed value
$\overline{X}$ = Average value

■ REFERENCES

(1) Ye, M.; Li, H.; Zhao, Y.; Zhang, T.; Liu, Z. MTO process development: The key of mesoscale studies. *Advances in Chem. Eng.* **2015**, *47*, 279−335.

(2) Alamolhoda, F.; Shamiri, A.; Hussain, M.; Zarghami, R.; Sotudeh-Gharebagh, R.; Mostoufi, N. Detection of agglomeration by analysis of vibration signatures in a pilot-scale fluidized bed reactor of propylene polymerization. *Int. J. of Chem. Reactor Eng.* **2019**, *17*, 2.

(3) Chmelar, J.; Matuska, P.; Gregor, T.; Bobak, M.; Fantinel, F.; Kosek, J. Softening of polyethylene powders at reactor conditions. *Chem. Eng. J.* **2013**, *228*, 907−916.

(4) Datta, S.; Sarkar, P.; Chavan, P.; Saha, S.; Sahu, G.; Sinha, K.; Saxena, V. Agglomeration behaviour of high ash Indian coals in fluidized bed gasification pilot plant. *Applied Thermal Eng.* **2015**, *86*, 222−228.

(5) Elled, A.; Åmand, L.; Steenari, B. Composition of agglomerates in fluidized bed reactors for thermochemical conversion of biomass and waste fuels. *Fuel* **2013**, *111*, 696−708.

(6) Zhong, Y.; Wang, Z.; Guo, Z.; Tang, Q. Prevention of agglomeration/defluidization in fluidized bed reduction of Fe$_2$O$_3$ by CO: The role of magnesium and calcium oxide. *Powder Technol.* **2013**, *241*, 142−148.

(7) Montes, A.; Ghiasi, E.; Tran, H.; Xu, C. Study of bed materials agglomeration in a heated bubbling fluidized bed (BFB) using silica

sand as the bed material and KOH to simulate molten ash. *Powder Technol.* **2016**, *291*, 178−185.

(8) Geldart, D. Types of gas fluidization. *Powder Technol.* **1973**, *7*, 285−292.

(9) Yang, W.-C. Modification and re-interpretation of Geldart's classification of powders. *Powder Technol.* **2007**, *171* (2), 69−74.

(10) Mostoufi, N. Revisiting classification of powders based on interparticle forces. *Chem. Eng. Sci.* **2021**, *229*, 116029.

(11) Botterill, J.; Teoman, Y.; Yuregir, K. The effect of operating temperature on the velocity of minimum fluidization bed voidage and general behavior. *Powder Technol.* **1982**, *31*, 101−110.

(12) Lucas, A.; Arnaldos, J.; Casal, J.; Puigjaner, L. High temperature incipient fluidization in mono and polydisperse systems. *Chem. Eng. Commun.* **1986**, *41*, 121−132.

(13) Lettieri, P.; Newton, D.; Yates, J. High temperature effects on the dense phase properties of gas fluidized beds. *Powder Technol.* **2001**, *120*, 34−40.

(14) Shabanian, J.; Chaouki, J. Fluidization characteristics of a bubbling gas−solid fluidized bed at high temperature in the presence of inter-particle forces. *Chem. Eng. J.* **2016**, *288*, 344−358.

(15) Fu, L.; Bai, H.; Bai, D.; Xu, G. Hydrodynamics of gas-solid fluidization at ultra-high temperatures. *Powder Technol.* **2022**, *406*, 117552.

(16) Cui, H.; Chaouki, J. Inter-particle forces in high temperature fluidization of Geldart A particles. *China Particuol.* **2004**, *2*, 113−118.

(17) Raso, G.; D'Amore, M.; Formisani, B.; Lignola, P. The influence of temperature on the properties of the particulate phase at Incipient fluidization. *Powder Technol.* **1992**, *72*, 71−76.

(18) Formisani, B.; Girimonte, R.; Mancuso, L. Analysis of the fluidization process of particle beds at high temperature. *Chem. Eng. Sci.* **1998**, *53*, 951−961.

(19) Chirone, R.; Poletto, M.; Barletta, D.; Lettieri, P. The effect of temperature on the minimum fluidization conditions of industrial cohesive particles. *Powder Technol.* **2020**, *362*, 307−322.

(20) Makkawi, Y.; Wright, P. Fluidization regimes in a conventional fluidized bed characterized by means of electrical capacitance tomography. *Chem. Eng. Sci.* **2002**, *57*, 2411−2437.

(21) Du, B.; Warsito, W.; Fan, L. ECT studies of the choking phenomenon in a gas-solid circulating fluidized bed. *AIChE J.* **2004**, *50*, 1386−1406.

(22) Li, X.; Jaworski, A.; Mao, X. Bubble size and bubble rise velocity estimation by means of electrical capacitance tomography within gas-solids fluidized beds. *Measurement* **2018**, *117*, 226−240.

(23) Guo, Q.; Meng, S.; Zhao, Y.; Ma, L.; Wang, D.; Ye, M.; Yang, W.; Liu, Z. Experimental verification of solid-like and fluid-like states in the homogeneous fluidization regime of Geldart A particles. *Ind. Eng. Chem. Res.* **2018**, *57*, 2670−2686.

(24) Ye, M.; Luo, Q.; Meng, S.; Zhang, T.; Liu, Z. An electrical capacitance tomography sensor withstanding high temperature and its fabrication method. Chinese Patent ZL201510623768.9, Sept. 25, 2015.

(25) Ye, M.; Guo, Q.; Meng, S.; Zhang, T.; Liu, Z. An electrical capacitance tomography sensor withstanding high temperature. Chinese Patent ZL201510967356.7, Dec. 18, 2015.

(26) Huang, K.; Meng, S.; Guo, Q.; Ye, M.; Shen, J.; Zhang, T.; Yang, W.; Liu, Z. High-temperature electrical capacitance tomography for gas−solid fluidized beds. *Meas. Sci. Technol.* **2018**, *29*, 104002.

(27) Wang, D.; Xu, M.; Marashdeh, Q.; Straiton, B.; Tong, A.; Fan, L. Electrical Capacitance Volume Tomography for Characterization of Gas−Solid Slugging fluidization with Geldart Group D Particles under High Temperatures. *Ind. Eng. Chem. Res.* **2018**, *57*, 2687−2697.

(28) Yang, W.; Peng, L. Image reconstruction algorithms for electrical capacitance tomography. *Meas. Sci. Technol.* **2003**, *14*, R1−R13.

(29) Kanada, T. Estimation of sphericity by means of statistical processing for roundness of spherical parts. *Precision Eng.* **1997**, *20*, 117−122.

(30) Liu, S.; Fu, L.; Yang, W. Optimization of an iterative image reconstruction algorithm for electrical capacitance tomography. *Meas. Sci. Technol.* **1999**, *10*, L37−L39.

(31) Huang, K.; Meng, S.; Guo, Q.; Yang, W.; Zhang, T.; Ye, M.; Liu, Z. Effect of electrode length of an electrical capacitance tomography sensor on gas−solid fluidized bed measurements. *Ind. Eng. Chem. Res.* **2019**, *58*, 21827−21841.

(32) Banaei, M.; van Sint Annaland, M.; Kuipers, J. A. M; Deen, N. G. On the accuracy of Landweber and Tikhonov reconstruction techniques in gas-solid fluidized bed applications. *AIChE J.* **2015**, *61*, 4102−4113.

(33) Shabanian, J.; Chaouki, J. Hydrodynamics of a gas−solid fluidized bed with thermally induced inter-particle forces. *Chem. Eng. J.* **2015**, *259*, 135−152.

(34) Xu, C.; Zhu, J. Effects of gas type and temperature on fine particle fluidization. *China Particuol.* **2006**, *4*, 114−121.

(35) Rhodes, M.; Wang, X.; Forsyth, A.; Gan, K.; Phadtajaphan, S. Use of a magnetic fluidized bed in studying Geldart Group B to A transition. *Chem. Eng. Sci.* **2001**, *56*, 5429−5436.

(36) Ye, M; van der Hoef, M.A; Kuipers, J.A.M A numerical study of fluidization behavior of Geldart A particles using discrete particle model. *Powder Technol.* **2004**, *139*, 129−139.

(37) Ye, M.; van der Hoef, M.A.; Kuipers, J.A.M. The effects of particle and gas properties on the fluidization of Geldart A particles. *Chem. Eng. Sci.* **2005**, *60*, 4567−4580.

(38) Rapagnà, S.; Foscolo, P.; Gibilaro, L. The influence of temperature on the quality of gas fluidization. *Int. J. Multiph. Flow* **1994**, *20*, 305−313.

(39) Rao, A.; Curtis, J.; Hancock, B.; Wassgren, C. The effect of column diameter and bed height on minimum fluidization velocity. *AIChE J.* **2010**, *56* (9), 2304−2311.

(40) Subramani, H. J.; Mothivel Balaiyya, M.B.; Miranda, L. R. Minimum fluidization velocity at elevated temperatures for Geldart's group-B powders. *Exp. Therm. Fluid Sci.* **2007**, *32*, 166−173.

(41) Wen, C.; Yu, Y. A generalized method for predicting the minimum fluidization velocity. *AIChE J.* **1966**, *12* (3), 610−612.

(42) Pattipati, R.; Wen, C. Minimum fluidization velocity at high temperatures. *Ind. Eng. Chem. Process Des. Dev.* **1981**, *20* (4), 705−707.

(43) Korkerd, K.; Soanuch, C.; Zhou, Z.; Piumsomboon, P.; Chalermsinsuwan, B. Correlation for predicting minimum fluidization velocity with different size distributions and bed inventories at elevated temperature in gas-solid fluidized bed. *Adv. Powder Technol.* **2022**, *33* (3), 103483.

(44) Escudero, D.; Heindel, T. Bed height and material density effects on fluidized bed hydrodynamics. *Chem. Eng. Sci.* **2011**, *66* (16), 3648−3655.

(45) Olofsson, G.; Ye, Z.; Bjerle, I.; Andersson, A. Bed agglomeration problems in fluidized-bed biomass combustion. *Ind. Eng. Chem. Res.* **2002**, *41* (12), 2888−2894.

(46) Castellanos, A.; Valverde, J.; Quintanilla, M. The Sevilla powder tester: a tool for characterizing the physical properties of fine cohesive powders at very small consolidations. *KONA Powder Part J.* **2004**, *22*, 66−81.

(47) Molerus, O. Theory of yield of cohesive powders. *Powder Technol.* **1975**, *12*, 259−275.

(48) Hsu, W.; Huang, A.; Kuo, H. Analysis of interparticle forces and particle-wall interactions by powder bed pressure drops at incipient fluidization. *Powder Technol.* **2018**, *325*, 64−68.

(49) Valverde, J.; Castellanos, A. Types of gas fluidization of cohesive granular materials. *Phys. Rev. E* **2007**, *75*, No. 031306.

(50) Jean, R.; Fan, L. On the model equations of Gibilaro and Foscolo with corrected buoyancy force. *Powder Technol.* **1992**, *72*, 201−205.

(51) Richardson, J.; Zaki, W. Sedimentation and fluidization. *Trans. Inst. Chem. Eng.* **1954**, *3* (2), 65.

(52) Oke, O.; Lettieri, P.; Mazzei, L. An investigation on the mechanics of homogeneous expansion in gas-fluidized beds. *Chem. Eng. Sci.* **2015**, *127*, 95−105.

(53) Agu, C.; Pfeifer, C.; Eikeland, M.; Tokheim, L.; Moldestad, B. Models for Predicting Average Bubble Diameter and Volumetric Bubble Flux in Deep fluidized Beds. *Ind. Eng. Chem. Res.* **2018**, *57*, 2658−2669.

(54) Shabanian, J.; Chaouki, J. Local characterization of a gas−solid fluidized bed in the presence of thermally induced interparticle forces. *Chem. Eng. Sci.* **2014**, *119*, 261−273.

(55) Ma, J.; van Ommen, J. R.; Liu, D.; Mudde, R. F.; Chen, X.; Wagner, E. C.; Liang, C. Fluidization dynamics of cohesive Geldart B particles. Part I: X-ray tomography analysis. *Chem. Eng. J.* **2019**, *359*, 1024−1034.

(56) Shabanian, J.; Chaouki, J. Effects of temperature, pressure, and interparticle forces on the hydrodynamics of a gas-solid fluidized bed. *Chem. Eng. J.* **2017**, *313*, 580−590.

(57) Yates, J. Effects of temperature and pressure on gas-solid fluidization. *Chem. Eng. Sci.* **1996**, *51*, 167−205.